Research Square

Preprints are preliminary reports that have not undergone peer review.
They should not be considered conclusive, used to inform clinical practice,
or referenced by the media as validated information.

Design of a GNSS Data Post-Processing Pipeline for Ionospheric TEC Mapping in the ELECTRA CubeSat Mission

Francesco Fiorina

francesco.fiorina@polito.it

Politecnico di Torino

Serena Campioli
Politecnico di Torino

Andrea Monagheddu
Politecnico di Torino

Alessandro Di Nuzzo
Politecnico di Torino

Paolo Cerutto
Politecnico di Torino

Ernesto Belluardo
Politecnico di Torino

Giorgio Abbate
Politecnico di Torino

Alessio Taretto
Politecnico di Torino

Claudio Cesaroni
Istituto Nazionale di Geofisica e Vulcanologia

Alex Minetto
Politecnico di Torino

Andrea Nardin
Politecnico di Torino

Fabio Dovis
Politecnico di Torino

Sabrina Corpino
Politecnico di Torino

Research Article

Keywords: Ionosphere, CubeSat, Global navigation satellite system, Navigation systems, Satellite technology, Navigation

Posted Date: November 12th, 2026

DOI: https://doi.org/10.21203/rs.3.rs-11435196/v1

License: This work is licensed under a Creative Commons Attribution 4.0 International License.
Read Full License

Additional Declarations: No competing interests reported.

Design of a GNSS Data Post-Processing Pipeline for Ionospheric TEC Mapping in the ELECTRA CubeSat Mission

Francesco Fiorina[1]*, Serena Campioli[2], Andrea Monagheddu[2], Alessandro Di Nuzzo[2], Paolo Cerutto[2], Ernesto Belluardo[2], Giorgio Abbate[2], Alessio Taretto[2], Claudio Cesaroni[3], Alex Minetto[1], Andrea Nardin[1], Fabio Dovis[1], Sabrina Corpino[2]

[1] *Department of Electronics and Telecommunications, Politecnico di Torino, Torino, Italy*
[2] *Department of Mechanical and Aerospace Engineering, Politecnico di Torino, Torino, Italy*
[3] *Istituto Nazionale di Geofisica e Vulcanologia, Roma, Italy*
**Corresponding author: francesco.fiorina@polito.it*

Abstract

ELECTRA is a 3U CubeSat mission developed at Politecnico di Torino by the CubeSat student team, in collaboration with the Systems and Technologies for Aerospace Research Laboratory (STAR Lab) and the NavSAS research group. The mission characterizes the topside ionospheric TEC in the LEO region by measuring dual-frequency GNSS signal excess path delays between the CubeSat receiver and GNSS satellites. Unlike ground-based sensing, limited to the bottomside up to the F2 peak, ELECTRA's onboard observables extend coverage above F2, enabling multilayer ionospheric mapping when combined with ground data. This supports a deeper understanding of topside ionosphere and plasmasphere dynamics and their response to space weather events, informing GNSS navigation and communication mitigation strategies. The mission represents an initial step toward an autonomous LEO ionospheric monitoring constellation, with ELECTRA serving as a pilot unit. It has attracted strong scientific interest in Italy, where INGV supports its development and plans to exploit its data, highlighting the growing role of CubeSats in advancing space weather science.

Keywords: Ionosphere, CubeSat, Global navigation satellite system, Navigation systems, Satellite technology, Navigation

1. Introduction

The ionosphere is a dispersive propagation medium for Global Navigation Satellite System (GNSS) signals. Its effect on radiofrequency signals is mainly driven by the electron density that integrated along the propagation path, gives rise to the Total Electron Content (TEC). TEC is therefore a key parameter for investigating ionospheric dynamics and assessing the impact of external forcing (e.g., space weather phenomenon, Litosphere-Atmosphere-Ionosphere coupling), improving ionospheric forecasting and the resilience of satellite navigation and communications. Ground-based Global Navigation Satellite System (GNSS) networks are widely used for ionospheric monitoring and Total Electron Content (TEC) mapping (Teunissen & Montenbruck, 2017) . However, their observation geometry is constrained by receiver-satellite ray paths terminating at the Earth's surface. Spaceborne GNSS observations provide a complementary geometry for investigating the topside ionosphere/plasmasphere and for improving GNSS-based ionospheric modeling (Ren, Chen, et al., 2020) , (Ren et al., 2022) , (Kashcheyev & Nava, 2019) , (Cesaroni et al., 2026).

In this context, small Low Earth Orbit (LEO) satellites represent a promising platform for GNSS-based ionospheric sensing. Their reduced cost and increasing technological capability make them suitable for demonstrating compact scientific payload and for assessing scalable architectures for future space-based monitoring system (Angling et al., 2021). CubeSat missions equipped with dual-frequency GNSS receivers can provide raw observables useful for TEC estimation, ionospheric irregularity assessment and, when the satellite configuration allows, radio-occultation-based electron density retrieval. An example of emblematic CubeSat mission is the Spire constellation (Angling et al., 2021) composed by hundreds of satellites orbiting the earth.

Under these assumptions, the Electron Layer Exploration using CubeSat for TEC Research and Analysis (ELECTRA) mission concept has been conceived by the CubeSat PoliTo team at Politecnico di Torino. Electron Layer Exploration using CubeSat for TEC Research and Analysis (ELECTRA) is a 3U CubeSat mission, designed to analyze and map the

ionospheric TEC using dual frequency GNSS signals acquired in Low Earth Orbit (LEO). Both Global Positioning System (GPS) and Galileo satellites will be acquired. The main scientific objective is therefore to detect and monitor TEC variations above its orbit during the mission. By leveraging the satellite's natural orbital decay, ELECTRA will study TEC variations at different altitudes, initially above and eventually below the F2 layer. This approach will provide a more comprehensive dataset across ionospheric layers, enabling a detailed examination of ionospheric behavior over time with high spatial resolution data. Therefore, the data on Earth could be compared with those in orbit below F2, together with an addition to the data measured only by CubeSat beyond F2, allowing for a multilayer mapping of the ionosphere. Specifically, ELECTRA's use of dual-frequency multi-constellation GNSS measurements will provide insights into the physical processes governing plasma exchange between the ionosphere and plasmasphere. This process is particularly significant during geomagnetic storms, when plasmasphere refilling plays a crucial role in the overall dynamics of the ionosphere.

In addition to TEC measurements, the mission will integrate data from GNSS Radio Occultation (RO) to derive electron density profiles up to the LEO satellite altitude (see Figure 1). This will enable the characterization of bottom side ionospheric structures as well (Ren, Zhang, et al., 2020) , (Ren, Chen, et al., 2020) , (Ren et al., 2022) , (Wu et al., 2022) , (Ren et al., 2021) , (L. Liu et al., 2022) . By leveraging this technique, the mission will determine key ionospheric parameters, such as the altitude of the F-layer peak (hmF2) and the maximum electron density (NmF2). These measurements will contribute to improving space weather models and forecasting, leading to the development of mitigation strategies that protect satellite communications and navigation systems from space weather disturbances (Kashcheyev & Nava, 2019) during severe space weather events. Meaningful TEC estimates and RO observations need to be associated to an accurate Position, Velocity and Time (PVT) solution; to this purpose Precise Orbit Determination (POD) is performed to enable precise ionospheric mapping. If from a scientific perspective, the rationale for a CubeSat mission targeting the ionosphere is evident, the educational perspective of such initiative is not to be forgotten: as a student-driven project, ELECTRA is intrinsically conceived as a low-cost mission, and this represents one of its key advantages. In this sense, ELECTRA serves as a proof of concept, providing a pioneering demonstration of whether low-cost CubeSat missions of this kind are both technically feasible and scientifically relevant, and opening the doors for a future constellation dedicated to global ionospheric monitoring.

Section 2 presents a thorough overview of the ELECTRA mission, covering the scientific and operational constraints that characterise it, together with a description of the dedicated GNSS payload selected to address them. The complete processing pipeline and its mathematical formulation are then detailed in Section 3. Finally, since this work focuses on the scientific goals of the mission, Section 4 outlines the planned validation steps that will consolidate the overall mission design. Therefore, this work presents the ELECTRA mission, the design gaps it proposes to address, and the data processing pipeline conceived to investigate ionospheric TEC in LEO using dual-frequency, multi-constellation GNSS measurements.

2. Mission and Data Context

2.1 ELECTRA mission overview

ELECTRA is a student-driven 3U CubeSat mission under development at Politecnico di Torino, Italy, by the CubeSat PoliTo team. The mission combines scientific, technological and educational objectives: its scientific goal is the analysis of ionospheric Total Electron Content (TEC) from LEO using dual-frequency GNSS measurements, while the technological objective is the in-orbit demonstration of a solid-state microthruster for CubeSat applications (Campioli et al., 2025) . In parallel, the mission provides students with hands-on experience in the full-lifecycle of a space mission development, from design to orbit, including direct operations through the CubeSat Control Center (C3) (Abbate et al., 2025) .

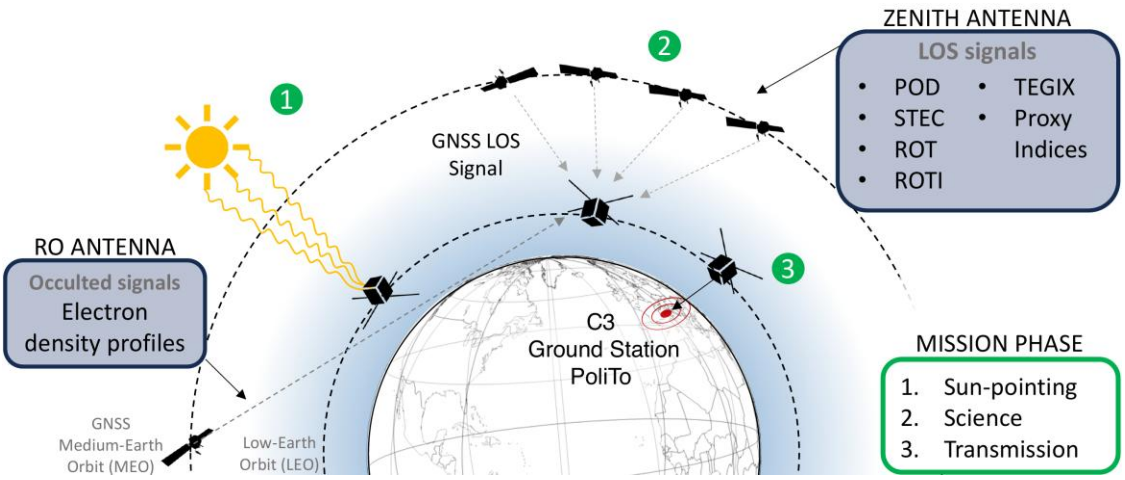


Fig. 1. ELECTRA Mission phases and scientific products

The baseline orbit is a near-circular Sun-Synchronous Orbit (SSO) at approximately 500 km altitude and 97.40° inclination. The orbit was selected as a compromise between scientific coverage, launch availability, ground-station access, and compliance with space debris mitigation constraints. The Sun-Synchronous Orbit (SSO) provides broad latitude coverage and repeated observations under comparable local-time conditions, which is particularly relevant for constructing a temporally consistent ionospheric dataset for later scientific studies.

The 3U spacecraft is equipped with two dual-frequency GNSS receivers, two GNSS antennas, an in-house Attitude and Orbit Control Subsystem (AOCS), a UHF and S-band communication subsystem, an Electrical Power Subsystem with deployable solar panels, an On-Board Data Handling (OBDH) system, and the solid-state micro-thruster. The spacecraft is designed as a compact GNSS sensing platform: the GNSS payload provides the observables required for TEC and electron density profile retrieval and POD, while the OBDH stores the science data before downlink. The system architecture, shown in Figure 2, is based mainly on a distributed onboard architecture, with subsystem communication relying primarily on Controller Area Network (CAN) bus and dedicated interfaces for payload data transfer.

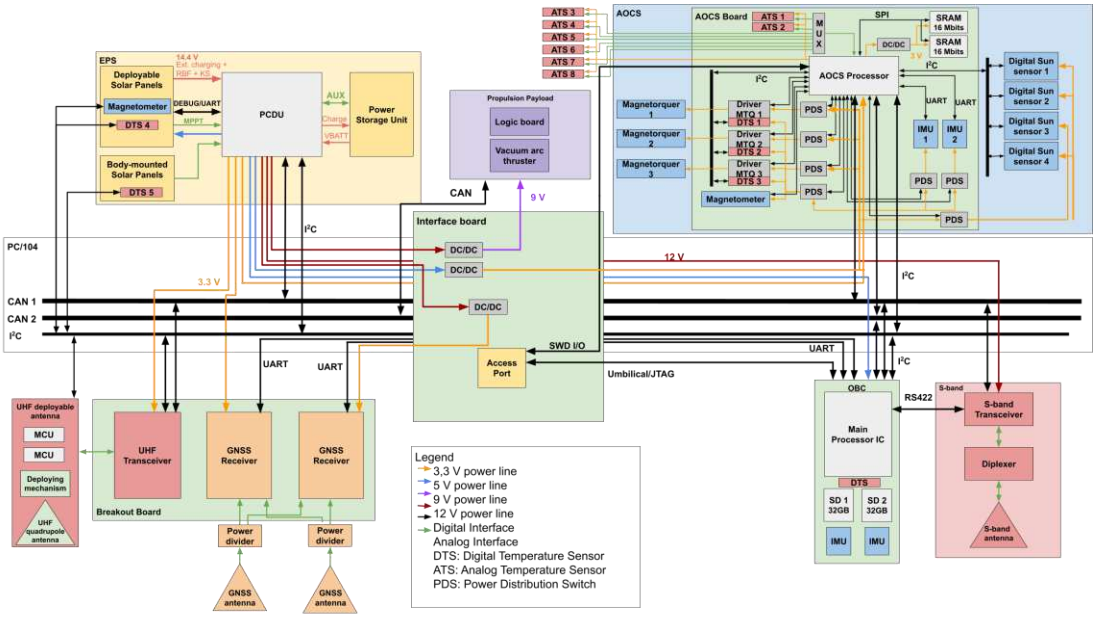


Fig. 2. ELECTRA system architecture

2.2 GNSS payload and observable acquisition

The GNSS payload includes two AsteRx-m3 Pro GNSS receivers and two TAOGLAS GVLB258.A GNSS Antennas.

The GNSS receivers are chosen for their high sample rate combined with low consumption, the dual-frequancy (L1/E1 and L5/E5a) capability necessary for TEC estimation, the multi-constellation (GPS and Galileo) feature and the compact format. The chosen receiver is dual-antenna capable so that is possible to acquire the GNSS signals from two different observation and orientation points. In particular, the second GNSS receiver is operating in cold redundancy so that if the first one fails then the second one can be turned on and operated.

The connection with the On-Board Computer (OBC) is guaranteed via one of the receiver's high-speed serial port Low Voltage Transistor-Transistor Logic (LVTTL), using the Universal Asynchronous Receiver/Transmitter (UART) protocol by leveraging the pass-through pins of the PC/104 bus. Since the receiver lacks a native PC/104 interface, it is integrated into the system PC/104 stack through a custom-designed breakout board.

The GNSS receivers are connected through a coaxial cable to the low profile, multi band patch antennas. One antenna will be mounted atop the UHF antenna, with the top cover plate modified to allow for its positioning. The coaxial cable will pass through the UHF antenna aperture in the structure, reaching the GNSS receiver. The other antenna will be mounted along the solar cells on the solar panel Printed Circuit Board (PCB). The coaxial cable will run along the inside of the satellite towards the other GNSS receivers. The connection from the antennas' coaxial cables to the receivers passes through a diplexer which splits the signal toward the two receivers and connection is guaranteed through a Micro-Miniature Bayonet X (MMBX) male connector. Even though both GNSS are capable of feeding 5VDC through the Radio Frequency (RF) cable, both antennas are passive hence this feature will not be used.

The Septentrio AsteRx-m3 Pro receiver provides a wide variety of Septentrio Binary Format (SBF) outputs (Septentrio nv/sa, 2023) ; however, only a specific subset is stored for subsequent downlink, POD computation and selected on the basis of direct relevance to the TEC science objectives. Table 1 lists these fields together with their bit allocation and scientific relevance. The Taoglas GVLB258.A antennas are dual-stacked ceramic patch antennas covering the GNSS frequency bands of interest. As depicted in Fig. 4, the two units are mounted orthogonally, with one aligned along the zenith direction and the other along the in-track direction, serving the POD and RO objectives respectively.

Table 1. Data budget for down-linked telemetry and its scientific use.

Field	**Bits**	**Science use**
Epoch header, once per epoch		
WNc	16	Absolute GPS week; time tag for all observables.
TOW	32	Time of week (0.001 s); epoch reference for RO, TEC, POD.
Master signal – MeasEpochChannelType1, one sub-block per tracked satellite per epoch		
RxChannel	8	Channel index; links master to its slave sub-blocks.
SVID	8	Satellite/constellation ID; mandatory for TEC pairing, RO attribution, Differential Code Bias (DCB).
Doppler	32	Carrier Doppler (10^{-4} Hz) of the master signal.
Misc (CodeMSB)	8	Upper 4 bits of pseudorange; completes the 36-bit PR word with CodeLSB.
CodeLSB	32	Master pseudorange (1 mm); reference for the dual-frequency Slant Total Electron Content (STEC) combination, POD, DCB.
CN0	8	C/N_0 (0.25 dB-Hz); quality gate for all science chains; S_4 proxy (Luo et al., 2020) .
CarrierLSB	16	LSB of master carrier phase (0.001 cyc); with CarrierMSB gives full phase for TEC, ROTI, RO.
CarrierMSB	8	MSB of master carrier phase (65.536 cyc/LSB); completes 1-mm-class phase observable.
ObsInfo	8	Bit 2: half-cycle ambiguity ($\pm\lambda/2 \approx 9.5$ cm on L1); bit 0: Hatch-smoothing active.
Slave signal – MeasEpochChannelType2, delta-encoded vs. master, one per epoch		
Type	8	Signal type + antenna ID; identifies the slave signal for dual-frequency pairing.
OffsetsMSB	8	Packed MSBs of ΔP and ΔD relative to master; required to decode secondary observables.
DopplerOffsetLSB	16	Reconstructs slave Doppler (10^{-4} Hz) via $D_{\rm slv}=\alpha D_{\rm mst}+\Delta D$; second-frequency Doppler for POD and cycle-slip check.

Field	Bits	Science use
CodeOffsetLSB	16	Reconstructs slave pseudorange (1 mm) via $P_{\rm slv}=P_{\rm mst}+\Delta P$; required for STEC and DCB estimation.
CN0	8	C/N_0 of slave signal; quality flag for the second-frequency track.
CarrierMSB	8	MSB of slave carrier phase; combined with CarrierLSB for TEC and ROTI.
CarrierLSB	16	LSB of slave carrier phase (0.001 cyc); completes the secondary phase observable.
Supplementary data – MeasExtra, one sub-block per signal (master and slave) per epoch		
DopplerVarFactor	64	$\sigma_D^2 = \text{CarrierVar} \times \text{DVF}$; formal Doppler weight for POD.
RxChannel	8	Links supplementary sub-block to the corresponding master/slave entry.
SmoothingCorr	16	Hatch-filter correction on the pseudorange; recovers raw PR; prevents smoothing bias in TEC/DCB.
MPCorrection	32	Multipath correction on the pseudorange; recovers unbiased PR for POD and code-phase TEC.
CodeVar	32	Code tracking noise variance; formal PR weight in POD least-squares.
CarrierVar	32	Carrier tracking noise variance; phase quality indicator for POD and RO QC.
Misc (CN0HighRes)	16	C/N_0 extended to 0.03125 dB-Hz; fine resolution for S_{4c} derivation (Luo et al., 2020) .
CumLossCont	8	Carrier phase cumulative loss-of-continuity counter. It starts at zero at receiver start-up, and is incremented at each initial (re)acquisition or whenever a cycle slip is detected; useful for Rate Of TEC (ROT) and Rate Of TEC Index (ROTI).
Onboard ECEF PVT, once per epoch (not per channel)		
x, y, z	3 × 64	ECEF position (f8, m); POD seed; RO geometry; TEC mapping function.
V_x, V_y, V_z	3 × 32	ECEF velocity (f4, m/s); a priori for kinematic POD; clock-drift check.
RxClkBias	64	Clock bias (f8, s); RO event time-tagging; zero-differencing in POD.
RxClkDrift	32	Clock drift (f4, s/s); jump detection; bias propagation between epochs.

2.3 Operational constraints for scientific data collection

The ELECTRA post-processing pipeline is constrained by the mission operational concept, since GNSS observables are not processed onboard but are acquired during dedicated science windows, stored in the onboard memory, downlinked to the ground segment, and then processed on ground. The mission operations are organized around a sequence of operating modes, shown in see Fig. 1 and Fig. 3, among which *Science Mode*, *Sun Pointing Mode*, and *Transmission Mode* are the most relevant for the scientific data chain.

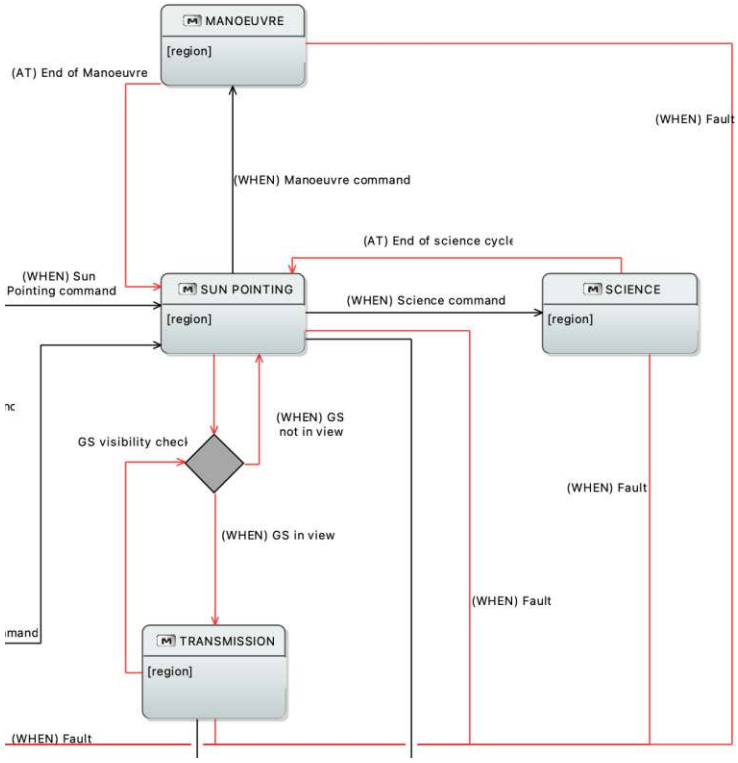


Fig. 3. ELECTRA Operative Modes - Focus on Science, Sun Pointing and Transmission Modes

During *Science Mode*, the GNSS payload is activated to collect the observables required for TEC retrieval, radio-occultation analysis, and POD. The acquired raw observables are stored by the OBC in the onboard mass memory, since their volume is not compatible with continuous real-time downlink through the low-rate communication link. To ensure reliable and scientifically relevant data, pointing requirements have been established to keep the payload antennas operating within their nominal Field Of View (FOV), guaranteeing undergrad signal reception. Taking Fig. 4 as a reference, Table 2 summarizes these requirements, derived from the antenna FOV of the most restrictive GNSS band, namely L5, as determined from the measured antenna radiation patterns at 0 dB. In particular it was considered the gain reduction due to a pointing offset α with respect to the boresight trough

$$L_c = -12\left(\frac{\alpha}{\theta}\right)^2 \tag{1}$$

where θ is the antenna half-power beamwidth and α is the pointing offset angle as in (Wertz et al., 2018) . In the design of the antenna pointing requirements losses in the antenna-to-receiver chain have been considered.

Table 2. Antenna FOV and pointing constraints by rotation axis.

Rotation	Plane	Science offset constraint	Driver
Pitch (about y)	XZ	$\pm 10°$	Conservative constraint
Roll (about x)	YZ	$\pm 10°$	Zenith POD antenna co-constraint
Yaw (about z)	XY	$\pm 30°$	Cross-track GPS access

Table 3 presents the maximum residual rotation rates allowable about Y (pitch axis). Rotation about X and Z are less restrictive, therefore the 0.128 rpm residual rotation rate of table 3 can be considered. These are derived from the FOV of the L5 band at 0 dBi gain and the minimum RO event duration T_{min}, according to:

$$\omega_{max} = \frac{FOV}{T_{min}} \tag{2}$$

Table 3. Maximum allowable spin rate as a function of the minimum RO integration time.

Science objective	$T_{\min}$ (s)	$\omega_{\max}$ (°/s)	$\omega_{\max}$ (RPM)	**Notes**
ROTI (threshold)	60	0.767	0.128	1 ROTI window (Kervalishvili et al., 2018)
Full RO profile (goal)	300	0.153	0.026	5 min (Leitinger et al., 1997)
Full RO pessimistic	540	0.085	0.014	9 min (Leitinger et al., 1997)

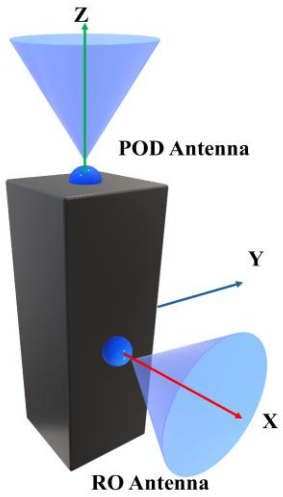


Fig. 4. Cubesat orientation: X is the in-track direction aligned with positive velocities, Y is the cross track direction and Z is the zenith pointing direction.

After a science acquisition window, the spacecraft transitions to Sun Pointing Mode. This mode is used to recover the energy consumed during payload operation and to maintain the platform in a safe and power-positive configuration before the next science or transmission opportunity. The alternation between *Science Mode* and *Sun Pointing Mode* is therefore a mission-level constraint that determines the temporal distribution of the available GNSS data.

Scientific data are downlinked during an on-ground planned transmission operation. The *Transmission Mode* is entered when a specific pre-planned command is received and the spacecraft is within the visibility window of the selected ground station. In this mode, the S-band link is used to transmit the stored payload data to the ground segment, while the UHF link remains available for basic telemetry and telecommand support. Raw GNSS observables, including pseudorange, carrier-phase-related fields, and clock information, are logged onboard and then transferred using a large-data-transfer service ST13, to ensure data integrity following ECSS-E-ST-70-41.

The downlinked data are received by the Ground Station at Politecnico di Torino, where the post-processing chain is executed. The available data products include pseudorange, pseudorange rate, timestamp, TEC estimates, carrier-to-noise density ratio C/N_0, and navigation data. These quantities support both the scientific processing, aimed at TEC and ionospheric irregularity retrieval, and the technical processing, aimed at POD and mission performance assessment. The sampling strategy is also linked to the operational concept. In particular, depending on both the ionospheric region (to keep it simple identified by the latitude) being sensed and the Local Time (LT) of the observation, it is possible to define a specific sampling strategy. Based on these two factors, the operational sampling strategy has been designed as summarized in Table 4. The parameter that varies with LT and latitude is the sampling frequency, driven by two principal considerations: the need for higher sampling rates to resolve small-scale or fast-moving irregularities, and the need to preserve onboard memory for scenarios where a lower sampling frequency is sufficient. In particular, a higher sampling frequency (10 Hz) is required whenever small-scale or fast-moving plasma irregularities are of interest, such as during the Pre-Reversal Enhancement (PRE) and post-sunset scintillation events at low latitudes, or during periods of Solar Wind-Magnetosphere-Ionosphere (SWMI) coupling at high latitudes. In the last column of Table 4 it is also specified whether a specific scenario has or not priority. As an example, if during the mission on-board memory is saturated then all the scenarios which have not any priority will not save and downlinked.

Table 4. GNSS sampling strategy by local time and latitude band.

Local Time (LT)	Latitude	Sampling Freq. (Hz)	Notes	Priority
02:00 – 06:00	Low (0° – ±30°)	10	Focus on small-scale irregularities (post-midnight scintillations).	Yes
06:00 – 10:00	Low (0° – ±30°)	1		No
10:00 – 14:00	Low (0° – ±30°)	1	Morphology of the Equatorial Ionization Anomaly (EIA) crests.	Yes
14:00 – 18:00	Low (0° – ±30°)	1		No
18:00 – 02:00	Low (0° – ±30°)	10	Focus on small-scale irregularities (PRE and post-sunset scintillations).	Yes
02:00 – 06:00	Mid (±30° – ±60°)	1		No
06:00 – 10:00	Mid (±30° – ±60°)	1		No
10:00 – 14:00	Mid (±30° – ±60°)	1		No
14:00 – 18:00	Mid (±30° – ±60°)	1		No
18:00 – 02:00	Mid (±30° – ±60°)	1		No
02:00 – 06:00	High (±60° – ±90°)	10	Small-scale irregularities induced by SWMI coupling.	Yes
06:00 – 10:00	High (±60° – ±90°)	10	=	Yes
10:00 – 14:00	High (±60° – ±90°)	10	=	Yes
14:00 – 18:00	High (±60° – ±90°)	10	=	Yes
18:00 – 02:00	High (±60° – ±90°)	10	=	Yes

ELECTRA is designed to provide measurements at a minimum rate of 1 Hz in the scientific regions of interest, while higher-rate acquisition can be used when needed to resolve small-scale ionospheric structures. The current baseline assumes that the receiver can acquire data at 10 Hz, with onboard down-sampling to 1 Hz when high-rate data are not required. It must be pointed out that to avoid the receiver reconfiguration, the down-sampling step will be operated by an OBC routine when necessary. This approach limits the onboard storage and downlink burden while preserving the capability to analyze fast or small-scale ionospheric variations during selected intervals.

2.4 Data budget

The data budget has been evaluated exploiting in house made MATLAB tools and GODOT, the Python astrodynamics library developed by European Space Agency (ESA) Flight Dynamics and used here for the propagation of ELECTRA. The analysis has been conducted under two bounding configurations:

1. A visibility mask corresponding to the most restrictive antenna FOV at 0 dBi, yielding a lower bound on the number of simultaneously visible satellites. This case also represents the most realistic scenario.

2. A 90° visibility mask, corresponding to the front hemisphere of each receiving antenna, representing the most demanding scenario in terms of total data volume.

Both analyzed configurations assume ideal pointing conditions, without accounting for the uncertainties listed in Table 2 and Table 3. Future work will address these aspects. Moreover, the ideal-pointing assumption guarantees the worst-case scenario in terms of maximum number of visible satellites, and hence the highest data volume. Since the selected receiver has an acquisition threshold of 33 dB-Hz, a link is considered viable only when $C/N_0 \geq 33$ dB-Hz. The antenna masks are not used as a replacement for the antenna gain patterns. In the link-budget evaluation, the receiver gain is computed from the Taoglas GVLB258.A patterns for the L1/E1 and L5/E5a bands, while the transmitter side is modelled using Galileo Galileo Reference Antenna Pattern (GRAP) E1/E5a patterns and GPS block-dependent transmit antenna patterns. The masks are then applied as geometric/operational filters on top of these pattern-based gains. For RO signals, an additional 3 dB margin is applied to account for dispersive ionospheric losses. Visibility analysis is used as the basis for the data budget estimation. The orbit is propagated with a fixed integration step of 10 s over 16 repeating cycles each consisting of 3 science orbits followed by 6 sun-pointing orbits that constitute the nominal operational pattern foreseen for the mission. The 16-cycle span is retained as the reference horizon for reporting, chosen as a compromise between simulation fidelity and computational cost. The data budget is evaluated epoch by epoch. The budget is sampled at 1 or 10 Hz depending on local time and latitude, specifically, results reported in this section are obtained under the Local Time of Ascending Node (LTAN) 23:00 reference condition, which represents the most demanding case among the analysed local-time configurations in terms of high-rate 10 Hz acquisition duration and, consequently, onboard data volume. Over each sampling interval the number of visible satellites is held constant, and each sampling interval is divided into sub sampling instants according to the sampling rate. The count is performed independently for the two antennas (the zenith-pointing POD antenna and the limb-pointing antenna used for RO) and on the two cases listed above. Therefore, the same GNSS satellite may contribute to both antennas if it is visible by both. The per-epoch payload, in bits, follows directly from the SBF encoding structure of Table 1:

$$B_{\text{epoch}} = H_{\text{epoch}} + \left(B_{\text{mst}} + B_{\text{sup}}\right)(x + y) \; + \left(B_{\text{slv}} + B_{\text{sup}}\right) y + B_{\text{PVT}}\, \mathbb{1}[\, x + y \geq 4\,] \tag{3}$$

where x is the number of satellites tracked on a single frequency and y the number tracked on both frequencies. The epoch header, H_{epoch}, is logged once per epoch. The master sub-block(B_{mst}, MeasEpochChannelType1) together with its supplementary record (B_{sup}, MeasExtra) is generated for every tracked satellite, hence the multiplier $(x + y)$; the slave sub-block (B_{slv}, MeasEpochChannelType2) with its own supplementary record applies only to dual-frequency satellites, hence the multiplier y. The PVT sub-block B_{PVT} is included only when the tracked geometry admits a navigation solution, i.e. when at least four distinct satellites are available ($x + y \geq 4$). Under this scenario, each science operations period produces approximately 0.774 Gbit/cycle of data in configuration 1 and 2.083 Gbit/cycle in configuration 2. Considering the most realistic case, namely case 1, the on-board memory (16 GB) would saturate after 165 science cycles. All this data is then downlinked to C3 considering two link scenarios depicted in Fig. 5: the optimistic one, which estimates a throughput of 2048 Kbps (1 access per science cycle for downlinking an entire science operation), and the pessimistic one, in which the link between ELECTRA and C3 closes at 512 Kbps (3-4 accesses per science cycle).

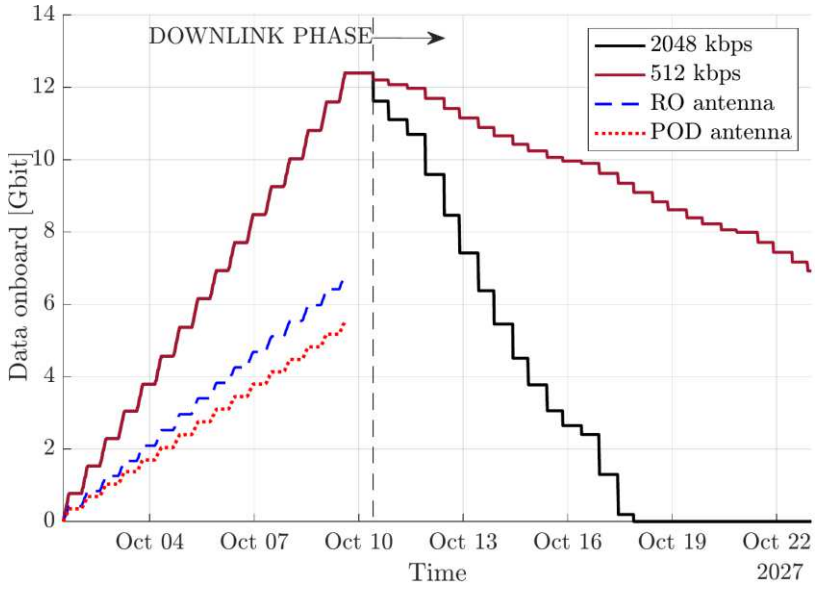


Fig. 5. On-board data storage and downlink scenarios for case 1.

From this kind of analysis can be also inferred when the scientific goals are satisfied, when the double frequency observables are present and the average number of GNSS satellites used for POD. Interesting observation can be done on Fig. 6, where the number of visible rising and setting occultation events is shown for a simulation of approximately 450 consecutive science orbits. Since the RO antenna is in track-pointing configuration, it sees on average ~2 satellites in dual frequency for rising events, while setting events are naturally less frequent. To observe setting events, the satellite must be oriented so that the RO antenna faces the anti-along-track direction.

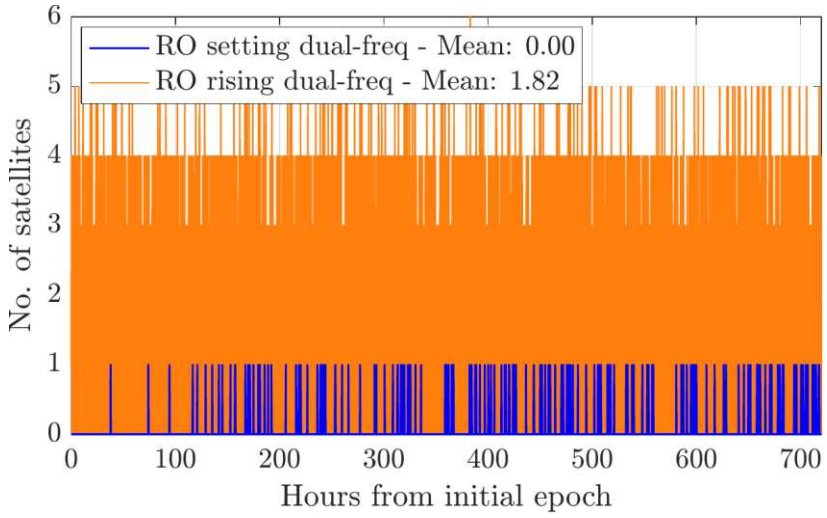


Fig. 6. Rising and Setting events in double frequency observed by RO antenna.

Regarding the POD zenith antenna, in scenario A, an average number of 8.66 GNSS satellites results to be visible for the entire simulation time. This is in line with other missions like Metop-A/B satellites being part of the European Organization for the Exploitation of Meteorological Satellites (EUMETSAT) polar system (Klaes et al., 2007) . Those satellites are performing POD with 8 active channels with a dual-frequency single constellation (GPS only) receiver (Innerkofler et al., 2020) . These operational constraints directly affect the design of the ground post-processing pipeline. The pipeline must handle data acquired in discrete arcs, possible gaps between acquisition and downlink, variable sampling rates, and different observations associated with the two antennas. For this reason, the processing chain includes steps for measurement selection, quality control, cycle-slip detection, smoothing or leveling, DCB calibration, and the generation of TEC-related products from non-continuous but temporally tagged GNSS observation arcs.

2.5 Design gaps

GNSS-based ionospheric sounding has its roots in the topside-sounder era inaugurated by the Alouette 1 mission in 1962 (Jackson, 1988) , though GNSS-specific techniques for topside characterization only emerged decades later. Since then, several space missions have contributed to the current understanding of the ionosphere. Many of these are summarized in Table 5, each characterized by different design choices. The table is divided into two parts: the upper section lists missions whose spacecraft are not miniaturized, as they carry onboard propulsion systems and accommodate several additional payloads; the lower section — in particular the last three rows — lists CubeSat missions.

As Table 5 shows, ELECTRA cannot compete against many of the missions listed, in terms of data volume, temporal coverage, or constellation size. However, at this stage the goal of ELECTRA is not to compete with established constellations such as Spire; rather, the objective is to test and validate strategies that have not yet been proposed onboard a 3U ionospheric-sounding CubeSat. In particular, the design gaps that ELECTRA aims to address are:

- A sounding rate scheduled *a priori* by LT and latitude band, prioritizing high-interest regions for fine STEC analysis while managing the onboard memory budget — as opposed to reactive, threshold-triggered high-rate acquisition as implemented on COSMIC-2.
- Ionospheric RO retrieval performed entirely on standard closed-loop observables (pseudorange and carrier phase) at up to 10 Hz, rather than on raw open-loop signal snapshots as required for neutral-atmosphere RO on missions such as Metop/GRAS and Spire. Since ELECTRA's RO objective is limited to ionospheric electron density retrieval, this observable-based approach avoids the corresponding onboard storage and downlink burden, independently of whether the flight receiver could support open-loop acquisition.
- Dual-constellation precise orbit determination (GPS + Galileo) from the zenith antenna, rather than the single-constellation, often semicodeless GPS tracking used by several legacy missions.
- A solid-state micro-thruster flown as a technology-demonstration payload, characterized in flight through the same GNSS science solution used for the mission's ionospheric measurements.

The design gaps presented above represent valuable technical and scientific strategies that could reduce costs, improve measurement robustness under constrained visibility geometries, and increase the autonomy of CubeSat missions.

Table 5. Comparative table: ELECTRA vs. other missions.

Mission	Orbit	GNSS signals	Antenna configuration	Sampling rate	Propulsion	Ionospheric yield / products
CHAMP (2000–2010) (Jakowski et al., 2002) , (Kuang et al., 2001) , (Reigber et al., 1999)	km; free decay	GPS L1/L2	1 zenith POD + 1 inclined 21° RO anti-velocity + 1 nadir GNSS-R	RO 1 Hz	Yes (cold gas)	TEC and RO profiles
Metop (2006–) (Klaes et al., 2007) , (Innerkofler et al., 2020) , (Montenbruck et al., 2013)	–884 km SSO mid-morning, $i = 98.7°$.	GPS L1 C/A, L1/L2 P(Y) (semi-codeless)	1 zenith (8 dual-freq. ch.) + 2 high-gain beam-forming (velocity ,anti-velocity , 2 ch. each)	POD 1 Hz; RO 50 Hz closed loop, 1 kHz open loop	Yes	~650 occultations/day , near-constant over the mission; RO and bending-angle products
GOCE (2009–2013) (Kervalishvili et al., 2018) , (Bock et al., 2007)	~255 km SSO; i = 96,5°	GPS L1/L2	Zenith POD antenna only (up to 12 simultaneous ch.)	Hz	Yes (ion)	Absolute STEC/VTEC and 1-min ROTI; no RO

Mission	Orbit	GNSS signals	Antenna configuration	Sampling rate	Propulsion	Ionospheric yield / products
Swarm A/B/C (2013–) (Cahuasquí et al., 2025) , (van den IJssel et al., 2016)	km (A/C), 530 km (B), $i \approx 88°$	GPS L1/L2 P	Zenith	Hz	Yes (cold gas)	STEC
CASSIOPE (2013–) (Montenbruck et al., 2019)	polar; 325×1500 km, $i = 81°$	GPS L1/L2	POD and attitude 4 zenith pointing; RO 1 anti velocity	Commandable 20 / 50 / 100 Hz	No	High-rate RO TEC inverted to N_e profiles; highest RO sampling rate flown to date
COSMIC-2 (2019–)(Straus, 2023), (Weiss et al., 2022), (Schreiner et al., 2020), (Ao et al., 2009)	s/c, 550 km, $i = 24°$; coverage $\pm 40°$ only	GPS + GLONASS operational (TGRS also capable of L5, E1/E5a)	2 choke-ring POD (ram/anti-ram, canted) + 2 beam-steering phased-array RO (ram/anti-ram)	POD 1 Hz, switched to high rate *when scintillation is detected on a link*; RO 50–100 Hz	Yes (liquid)	>5000 RO profiles/day; ~10 000 TEC estimates/day
Spire LEMUR-2 (2015–) (Angling et al., 2021) **CUBESAT**	–600 km, from equatorial to SSO	GPS / GLONASS / Galileo / QZSS / Beidou (L1/L2/L5)	1 zenith POD + 1 velocity + 1 anti-velocity	POD 1 Hz closed loop; RO 50 Hz open loop	Yes, since 2022 (iodine cold gas)	~9×10^6 TEC obs/day at 1 Hz; ~4000 relative RO profiles/day; ~90 min median latency; POD antenna: GPS only.
SCION (concept, not flown), (Heine et al., 2015) **CUBESAT**	–600 km, $i =$ 40–60°	GPS L1/L2	2 opposite patches scanning around zenith axis at 0.3 RPM	–50 Hz, (side-scan high rate, limb 0.1 Hz)	No	Multipoint TEC and S_4
ELECTRA (launch Q2 2027) **CUBESAT**	km SSO, $i =$ 97.40°; free decay	GPS L1/L5 + Galileo E1/E5a	1 zenith POD + 1 limb antenna in velocity direction	Hz baseline, 10 Hz *scheduled a priori by local time and latitude band*	Yes — solid-state micro-thruster as *technology-demonstration payload*	STEC/VTEC, ROT/ROTI, TEGIX, N_e profiles fom rising RO events

3. Methodology

3.1 Ionosphere characterization in the 3U ELECTRA mission

TEC is a key parameter that must be considered for various applications, including space weather forecasting and the study of geophysical phenomena. It is defined as the integral of the electron density along the ray path L from the transmitter to the receiver:

$$\mathrm{STEC} = \int n_\mathrm{e}\,\mathrm{d}l = -\frac{f^2}{40.3}\int (n-1)\,\mathrm{d}l \tag{4}$$

where n_e is the electron density, f is the radio wave frequency, and n is the refractivity index of the ionospheric medium.

Equation (4) is used to retrieve the STEC, which corresponds to the slant total electron content along the signal path. Then, by applying an appropriate mapping function to the STEC, it is possible to estimate

$$\mathrm{VTEC} = \frac{\mathrm{STEC}}{M(E)} \tag{5}$$

where VTEC denotes the Vertical Total Electron Content (VTEC), representing the total electron content directly above the antenna's zenith. It is commonly used in ionospheric correction models for single-frequency GNSS receivers(Teunissen & Montenbruck, 2017). The term $M(E)$ denotes the mapping function, which maps the STEC to the Ionospheric Piercing Points (IPP).

The IPP is defined as the point where the GNSS ray path intersects a hypothetical ionospheric shell of radius R_{shell}. This shell is commonly assumed to represent the entire ionosphere, simplifying it as a 2D distribution of electron content at a fixed height, typically within the range $350\,\mathrm{km} \leq R_{\mathrm{shell}} \leq 450\,\mathrm{km}$ (Teunissen & Montenbruck, 2017), (Hernández-Pajares et al., 2005). However, alternative mapping functions exist that avoid this thin-shell simplification, such as the one presented in (Hernández-Pajares et al., 2005).

Both the STEC and the VTEC are commonly expressed in Total Electron Content Units (TECU), where $1\ TECU = 10^{16}$ electrons/m^2.

In Equation (4), the refractive index plays a crucial role. This parameter is determined not only by the free electron density but also by the frequency of the radio signal. Therefore, it establish the frequency-dependent nature of the TEC measurement. As a result, the ionosphere—acting as a dispersive medium—affects signals of different frequencies in distinct ways.

The observables' processing pipeline is schematized in Fig. 7 and described in the following subsections.

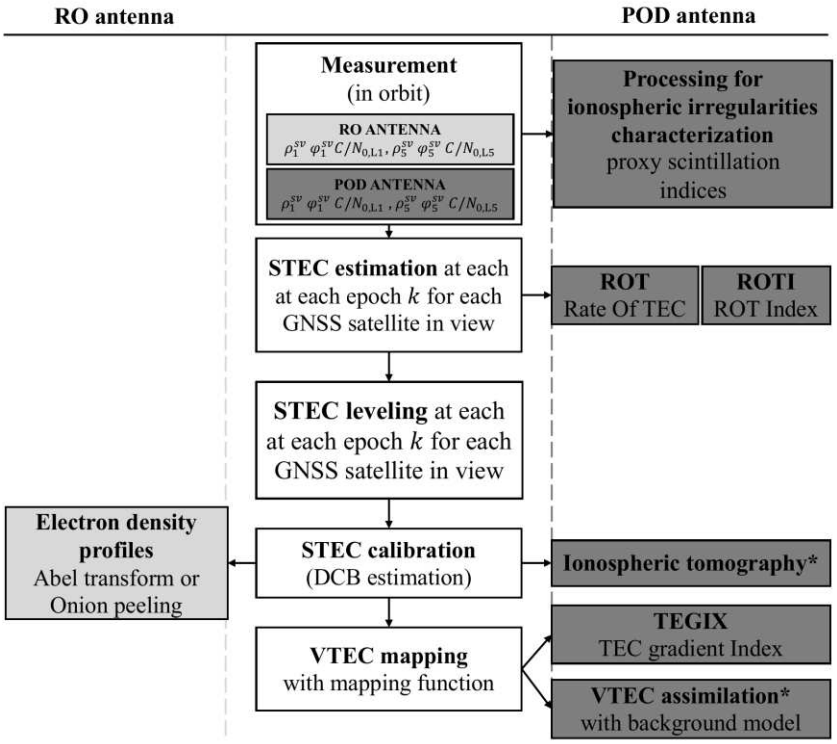


Fig. 7. Observables processing pipeline.

3.2 STEC estimate from GNSS measurements

GNSS signals do not travel through a vacuum but rather propagate through the ionosphere. This is particularly significant for signals received by the RO antenna, which traverse the ionosphere for up to 32% of the total ray path length — obtained as the ratio between the ionosphere-pierced path and the maximum ELECTRA–GNSS distance, computed for a ray tangent to the lower ionospheric boundary. The ionosphere is considered lying between 80 km and 1500 km (Morton et al., 2020). As a result, the signal propagation velocity is modified along the transmission path. Specifically, the group velocity is reduced, while the phase velocity is increased (Teunissen & Montenbruck, 2017). The first effect affects in turn the pseudorange measurements which, for each satellite, can be quantified through

$$\rho_{f_i} = \rho^* + \frac{40.3 \cdot \mathrm{STEC}}{f_i^2} + b_{r,i} - b_{sv,i} \tag{6}$$

while the second has an impact on the phase measurements

$$\varphi_{f_i} = \varphi^* - \frac{40.3 \cdot \mathrm{STEC}}{f_i^2} + \lambda_i n_i + b_{r,i} - b_{sv,i} \tag{7}$$

where ρ^* and φ^* are the iono-free pseudorange and phase from the receiver to a specific GNSS satellite, respectively. In particular, in both (6) and (7) are present the receiver and the satellite instrumental delays $b_{r,i}$ and $b_{sv,i}$. Similarly, (7) presents the integer ambiguity $N_i = \lambda_i n_i$. By leveraging the frequency-dependent nature of ionospheric effects, it is possible to estimate the STEC by applying a linear combination of two pseudorange or phase measurements acquired at different frequencies from the same GNSS satellite. This results in

$$\mathrm{STEC}_\rho = -\frac{f_1^2 f_f^2}{40.3\left(f_1^2 - f_f^2\right)}\left(\Delta\rho + \mathrm{DCB}_{1f,r} - \mathrm{DCB}_{1f,sv}\right) \tag{8}$$

or

$$\mathrm{STEC}_\varphi = \frac{f_1^2 f_f^2}{40.3\left(f_1^2 - f_f^2\right)}\left(\Delta\varphi + \mathrm{IFB}_{1f}\right) \tag{9}$$

Here, $f_1 = 1575.42$ MHz (*L1*), and f_f is another GNSS frequency—commonly: *L2 = 1227,60* MHz (as done for the Spire constellation (Angling et al., 2021)) or *L5 = 1176,45* MHz. For the ELECTRA mission,the L1/L5 (GPS) and E1/E5a (Galileo) combinations are adopted, this larger frequency separation improves ionospheric sensitivity and reduces TEC estimation noise (Jin, 2012). From this point forward, the second frequency is denoted with subscript "5". The other parameters in (8) and (9) are $\Delta\rho = \rho_1 - \rho_5$, $\Delta\varphi = \varphi_1 - \varphi_5$ containing also the ambiguities, while $\mathrm{DCB}_{15,r} = b_{r,5} - b_{r,1}$ and $\mathrm{DCB}_{15,sv} = b_{sv_5} - b_{sv,1}$ are the DCB terms resulting from the combination of double frequency observables, finally IFB_{1f} are the phase IFBs.

Besides the IFBs, the STEC derived from carrier phase measurements, $STEC_\varphi$, offers higher precision due to the lower noise level of phase observations. However, it includes phase ambiguities that must be estimated. In contrast, the STEC derived from code measurements, $STEC_\rho$, is less precise because it is more affected by multipath and other disturbances (Angling et al., 2021) , but it is unambiguous and provides absolute values.

3.3 STEC leveling

To obtain an accurate and precise STEC estimate, two main approaches can be considered: using phase measurements after ambiguity resolution or applying specific leveling techniques.

The first approach, based on ambiguity resolution, provides high precision but comes at a higher computational cost due to the need to estimate integer ambiguities. In contrast, the leveling approach is widely adopted as it achieves a good level of precision with significantly reduced computational effort.

The two main existing techniques are:

Raw measurement smoothing

This technique combines raw pseudorange measurements with carrier-phase measurements (Hatch, 1982), effectively reducing the noise on the code observations. Over the years, this method has been improved by introducing a Smoothing Weighting Factor (SWF), as discussed in (Hatch, 1986), and by scaling this factor based on the number of GNSS observations used during the smoothing process (Lachapelle et al., 1986).

Once the smoothing process is completed, then is possible to retrieve the STEC estimate by applying (8) for each epoch k, specifically by using the smoothed pseudoranges ρ_k^{sm} in place of the raw measurement.

TEC estimate leveling

In this approach the leveling step occurs only after the computation of (8) and (9) with the raw measurements. Between the two estimates there exists an offset that for the estimate at the k^{th} epoch can be quantified trough $\Delta\mathrm{STEC}_k^{sm}$ which is the leveled difference between (8) and (9).

In general, if ambiguities are constant over the entire signal tracking and no cycle slips occurs, then this difference is constant.

Now, by applying the recursion presented in (Skone, 1998), is possible to refine this first $\Delta\mathrm{STEC}_k$ estimate.

Finally, the refined offset, is then summed to (9) to obtain the leveled STEC.

Note that, by construction of the estimated offset, the IFB_{15} term appears with opposite sign in $\mathrm{STEC}_{\varphi,k}$ and $\Delta\mathrm{STEC}_k^{sm}$, and therefore cancels, leaving only the DCB term. It is important to remark that every time a cycle slip is detected the algorithm is reinitialized.

Leveling precision

The standard deviation of the STEC estimates can be computed by applying the closed-form expressions presented in (Z. Liu et al., 2005). The two leveling approaches described above are characterized by different variance propagation models.

Evaluating the standard deviation of the STEC estimates thus provides a direct assessment of the performance of the two leveling methods. In particular, it is shown that the approach described in Section 3.3.2 outperforms the method presented in Section 3.3.1. Specifically, the former demonstrates an exponential improvement in the precision of the STEC estimate as the leveling window increases. Based on this consideration, the method described in 3.3.2 is adopted in the processing pipeline.

3.4 STEC DCBs calibration

Notice that up to this point no corrections about DCBs has been considered. Specifically , at this point is possible to end up in different scenarios.

Known DCBs

In this case $\mathrm{DCB}_{15,r}$ and $\mathrm{DCB}_{15,sv}$ are known quantities from external sources. As an example, the GNSS satellites DCBs can be retrieved as precise products from the International GNSS Service (IGS) while from the receiver side the DCB correction is taken from the receiver itself. In this case the biases can be directly compensated in (8) and (9). In particular, the DCBs are estimated with a given uncertainty that can be considered in the STEC precision estimation and is assumed to be independent with respect to the STEC estimation process. At this point, the STEC also needs to take into account the DCB estimation uncertainty.

Unknown receiver's DCB

In this case, the receiver DCB must be estimated, while the satellite differential code bias $\mathrm{DCB}_{15,sv}$ can be retrieved from IGS products. The TEC calibration procedure models the corrected STEC by simultaneously estimating both the DCBs and the model parameters. For each epoch k, the STEC relates to the modeled value through:

$$\mathrm{STEC}_k = \mathrm{STEC}_k^{\mathrm{corr}} + \mathrm{DCB}_{15,r} - \mathrm{DCB}_{15,sv} \tag{10}$$

where the corrected STEC is given by:

$$\mathrm{STEC}_k^{\mathrm{corr}} = M(E) \cdot \mathrm{VTEC}_k^{\mathrm{corr}} \tag{11}$$

Here $\mathrm{VTEC}_k^{\mathrm{corr}}$ is the corrected VTEC and $M(E)$ is a mapping function. For instance, (Ren, Chen, et al., 2020) models $\mathrm{VTEC}_k^{\mathrm{corr}}$ using spherical harmonic expansion and employs the mapping function (Foelsche & Kirchengast, 2002) for $M(E)$.

The unknown $\mathrm{DCB}_{15,r}$ and the model parameter can be estimated through a least-squares:

$$\mathbf{y} = \mathbf{H}\mathbf{x} + \boldsymbol{\varepsilon}, \quad \text{with} \quad \boldsymbol{\varepsilon} \sim \mathcal{N}(0, \mathbf{R}) \tag{12}$$

where $\mathbf{y}$ is the vector of the STEC observations at a given epoch k, $\mathbf{H}$ is the design matrix, $\hat{\mathbf{x}}$ is the vector of the estimates and $\mathbf{R}$ is the covariance matrix associated to the STEC estimates coming out of the leveling process. The covariance matrix $\mathbf{R}$ is constructed using the STEC variances depending on the selected leveling method. A key aspect to note is that while the receiver's DCB remains unknown, only the satellite DCB appears under the square root in these calculations. The Weighted Least Square (WLS) estimate of the parameter vector $\mathbf{x}$ is given by:

$$\hat{\mathbf{x}} = (\mathbf{H}^\top \mathbf{W}\mathbf{H})^{-1}\mathbf{H}^\top \mathbf{W}\mathbf{y} \tag{13}$$

where $\mathbf{W} = \mathbf{R}^{-1}$ is the weight matrix. The weights may be defined as a function of the satellite elevation angle or with respect to the STEC precision.

In this specific case, it is important to consider that the DCB_r is estimated with a certain uncertainty. Notably, since the DCB estimation process depends on the uncertainties of the uncalibrated STEC, a correlation phenomenon exists, implying that covariances must be accounted for. The covariance matrix of the estimated parameters is given by:

$$\boldsymbol{\Sigma}_{\hat{\mathbf{x}}} = \mathbf{P} = (\mathbf{H}^\top \mathbf{W}\mathbf{H})^{-1} \tag{14}$$

To compute the variance of the corrected STEC:

$$\mathbf{Cov}(\mathrm{VTEC}^{\mathrm{corr}}) = \mathbf{R} - \mathbf{H}\mathbf{P}\mathbf{H}^\top \tag{15}$$

Since the estimated $\mathrm{DCB}_{15,r}$ remains stable over 24 hours (Ren, Chen, et al., 2020) , it can be treated as a constant for the entire day. As a result, estimating $\mathrm{DCB}_{15,r}$ once every 24 hours is sufficient. At the same time, the model coefficients used in corrections may need to be updated more frequently (e.g., every two hours) (Ren, Chen, et al., 2020) . Therefore, it is feasible and even beneficial to estimate the receiver DCB at the same frequency as the model updates.

Improved ZERO TEC Method

A simple and fast method for estimating $\mathrm{DCB}_{15,r}$ is the one proposed in (Zhong, Lei, Yue, et al., 2016), which assumes that during the night the STEC is approximately zero. In particular, given the measurement model:

$$\mathrm{STEC}_k = \mathrm{STEC}_k^{\mathrm{abs}} + \mathrm{DCB}_{15,r} - \mathrm{DCB}_{15}^{\mathrm{sv}} \tag{16}$$

where $\mathrm{STEC}_k^{\mathrm{abs}}$ is the absolute value of the STEC, the following is defined:

$$\mathrm{STEC}_k^r = \mathrm{STEC}_k^{\mathrm{abs}} + \mathrm{DCB}_{15,r} \tag{17}$$

which is the *relative* STEC, i.e., the k^{th} observation corrected for the satellite DCB.

Next, considering the ascending and descending arcs of the LEO satellite carrying the GNSS receiver, the minimum value of STEC for each orbit (ascent or descent) is selected. Since a LEO satellite completes about 15 revolutions per day (Zhong, Lei, Yue, et al., 2016), this results in 15 values each for ascending and descending passes. Then, for both ascending and descending sets, the 25th percentile (i.e., the lower quartile) of these minimum STEC values is computed:

$$\mathrm{STEC}_{lqmin}^r = \min\left(\mathrm{STEC}_{lqmin,ASC}^r, \mathrm{STEC}_{lqmin,DESC}^r\right) \tag{18}$$

Assuming that during nighttime $\mathrm{STEC}^{\mathrm{abs}} = 0$, it follows that:

$$\mathrm{STEC}_{lqmin}^r = \mathrm{DCB}_{15,r} \tag{19}$$

To improve data quality, an elevation mask of 40° is applied to exclude low-elevation observations.

However, this estimation can be biased by the plasmaspheric contribution. A correction offset, denoted as μ_0, is introduced. It represents the mean of the Gaussian distribution fitted over all the daily offsets μ_{daily} calculated during the entire study period. Each daily offset is defined as:

$$\mu_{\text{daily}} = \text{STEC}^r_{lqmin} - \text{STEC}^r_{dailymin} \tag{20}$$

The final corrected estimate of the receiver DCB is then given by:

$$\text{DCB}_{15,r_0} = \mu_0 + \text{DCB}_{15,r} \tag{21}$$

This offset μ_0 is applied uniformly to all daily estimates of $\text{DCB}_{15,r}$ throughout the analysis period.

The estimation of the variance of the corrected STEC, denoted as $\sigma^2_{\text{STEC}^{\text{corr}}_k}$, is not straightforward unless an assumption is made regarding the statistical independence between STEC^r_k and $\text{DCB}_{15,r}$. If one assumes that STEC^r_k and $\text{DCB}_{15,r}$ are independent, then the variance can be conservatively approximated by:

$$\sigma^2_{\text{STEC}^{\text{corr}}_k} = \sigma^2_{\text{STEC}^r_k} + \sigma^2_{\mu_0} + \sigma^2_{\text{DCB}_{15,r}} \tag{22}$$

This assumption simplifies the error propagation and results in a more conservative estimate of the corrected STEC uncertainty. However, if there is a correlation between the relative STEC values and the estimated DCB (as can happen when the DCB is derived from the same set of STEC measurements), the covariance term must be included. In that case, the corrected variance becomes:

$$\sigma^2_{\text{STEC}^{\text{corr}}_k} = \sigma^2_{\text{STEC}^r_k} + \sigma^2_{\mu_0} + \sigma^2_{\text{DCB}_{15,r}} - 2\,\text{Cov}\left(\text{STEC}^r_k,\ \text{DCB}_{15,r}\right) \tag{23}$$

A bootstrapping approach can be employed to estimate the covariance term $\text{Cov}\left(\text{STEC}^r_k, \text{DCB}_{15,r}\right)$ from the data of the same day. This method provides a more accurate and less conservative uncertainty estimate compared to the simplified uncorrelated assumption in (22).

Regarding the receiver DCB estimation both the strategies described in 3.4.2 and 3.4.3 are adopted. In particular, the latter is adopted to rapidly estimate the wanted quantity during preliminary analysis while the former is adopted whenever a more accurate estimation is necessary.

3.5 VTEC mapping

VTEC mapping represents the final processing step of the POD, consisting of a projection of the STEC estimates through (5), where $M(E)$ denotes the mapping function. Several mapping functions have been proposed in the literature to address specific observational geometries. In particular, (Zhong, Lei, Dou, et al., 2016), (Cheng & Morton, 2025) discuss the appropriate choice of mapping function for LEO-based GNSS data, where the selection depends on the elevation angle E of the GNSS signal.

Two mapping functions, dependent on R_{IEH} (the geocentric radius of the Ionospheric Effective Height (IEH)), R_{LEO} (the orbital radius), and the elevation angle E, are considered: the Foelsche and Kirchengast (F&K) mapping function (Foelsche & Kirchengast, 2002), used in conjunction with the centroid IEH,

$$M_{\text{F\&K}} = \frac{1 + R_{\text{IEH}}/R_{\text{LEO}}}{\sin E + \sqrt{(R_{\text{IEH}}/R_{\text{LEO}})^2 - \cos^2 E}} \tag{24}$$

and the Thin Layer Model (TLM) mapping function,

$$M_{\text{TLM}} = \frac{1}{\sqrt{1 - \left(\frac{R_{\text{LEO}}}{R_{\text{IEH}}}\right)^2 \cos^2 E}} \tag{25}$$

which is conventionally adopted for ground-based observations, used here together with the integral mean value of the IEH. The selection threshold between the two is set at $E = 40°$. When $E \geq 40°$, the F&K mapping function yields lower

errors compared to the TLM, as assessed through model-based simulations (Zhong, Lei, Dou, et al., 2016). Conversely, when $E < 40°$, the TLM is adopted alongside the integral mean value of the IEH.

3.6 Scientific products

Beyond the calibrated STEC and its vertical projection, additional ionospheric information can be extracted depending on the antenna source, enabling several analyses as depicted in Fig. 7.

POD Antenna

Observables from the POD antenna follow the full processing chain down to the VTEC mapping. A first analysis that can be performed directly from these observables is the characterisation of ionospheric irregularities through the S_4 scintillation index. In general, this index is computed from raw signal samples; however, since only receiver outputs are available here, a proxy scintillation index can be derived from the C/N_0 estimate (Luo et al., 2020) . Specifically, the index is computed as

$$S_{4C} = \sqrt{\frac{\langle SI_{\text{det}}^2 \rangle - \langle SI_{\text{det}} \rangle^2}{\langle SI_{\text{det}} \rangle^2}}, \tag{26}$$

where $\langle \cdot \rangle$ denotes the time average over a (Teunissen & Montenbruck, 2017), and SI_{det} is the detrended signal intensity derived from C/N_0 as

$$SI_{\text{det}}(k) = \frac{10^{0.1\,C/N_0(k)}}{\langle \sum_{i=1}^{n} 10^{0.1\,C/N_0(k-i)} \rangle}, \qquad k > n, \tag{27}$$

where k denotes the current epoch index and n is the number of samples within the averaging window (e.g. $n = 60$ for a 1-Hz receiver), and quantifies the intensity of the scintillation event. Unlike the classical S_4 index, this proxy may struggle to resolve very small-scale fluctuations due to its lower sample rate. However, as demonstrated in (Luo et al., 2020) , S_4 and S_{4c} show a high correlation coefficient even during strong scintillation events. Moreover, in (Luo et al., 2020) the S_{4c} index was computed using a 1 Hz sample rate; ELECTRA, by contrast, is designed to sample at higher rates, thus narrowing the gap with respect to the raw-sample-based classical index.

A complementary proxy index computable from the available observables is the phase fluctuation index σ_φ, defined as the standard deviation of the detrended signal phase over a sliding window of n samples:

$$\sigma_\varphi = \sqrt{\frac{1}{n-1} \sum_{k=1}^{n} (\varphi_k - \langle \varphi \rangle)^2}, \tag{28}$$

where φ_k is the k-th phase sample and $\langle \varphi \rangle$ is the mean phase over the window. As for S_{4C}, the index is conventionally evaluated over a 1-minute interval.

Once the uncalibrated STEC estimate is available, it is possible to compute its time derivative, known as the ROT, and its standard deviation over a sliding window, known as the ROTI. Both quantities are preferably derived from the phase-based estimate STEC_φ, as carrier-phase measurements are less noisy than code-based ones. It should be noted, however, that cycle slips produce spurious spikes in the ROT time series and consequently inflate ROTI (Luo et al., 2020) . The ROT is defined as

$$\text{ROT}_k = \frac{\text{STEC}_k - \text{STEC}_{k-1}}{t_k - t_{k-1}}, \tag{29}$$

and is particularly useful for identifying plasma bubbles and large-scale ionospheric gradients (Teunissen & Montenbruck, 2017) . The ROTI is defined as the standard deviation of the ROT over a prescribed window:

$$\mathrm{ROTI}_k = \sqrt{\frac{1}{N}\sum_{n=k-N/2}^{k+N/2-1}\left(\mathrm{ROT}_n - \overline{\mathrm{ROT}}\right)^2}, \tag{30}$$

where $\overline{\mathrm{ROT}}$ is the mean ROT over the window of N samples. It is conventionally evaluated over a 1 minute window at 1 Hz sampling, or equivalently over a 5-minute window at 30 s sampling (Teunissen & Montenbruck, 2017), (Luo et al., 2020), (Kervalishvili et al., 2018) , and is usually adopted as a proxy for small-scale ionospheric fluctuations.

Once the final processing step, the VTEC mapping, has been completed, it becomes possible to compute the TEC Gradient Index (TEC Gradient Index), (Cahuasquí et al., 2025) . This index characterizes horizontal TEC gradients in the topside ionosphere by forming gradient dipoles between pairs of IPPs associated with the same GNSS satellite. For each pair of pierce points IPP_i and IPP_j, separated by a distance Δs_{ij}, the gradient vector is estimated at the central point CP_{ij} and decomposed into its zonal (West-East) and meridional (South-North) components as

$$\nabla\mathrm{TEC}_{X,ij} = \frac{\mathrm{VTEC}_i - \mathrm{VTEC}_j}{\Delta s_{ij}}\sin\delta_{ij}, \tag{31}$$

$$\nabla\mathrm{TEC}_{Y,ij} = \frac{\mathrm{VTEC}_i - \mathrm{VTEC}_j}{\Delta s_{ij}}\cos\delta_{ij}, \tag{32}$$

where δ_{ij} is the azimuthal direction of the dipole measured clockwise from North. Depending on Δs_{ij} it is possible to analyse different phenomena, for example in (Cahuasquí et al., 2025) are only used pairs with separations in the range 30 km -200 km, enabling the detection of medium-scale ionospheric perturbations. TEC Gradient Index is particularly sensitive to ionospheric structures associated with plasma bubbles at low latitudes and ionization patches at high latitudes (Cahuasquí et al., 2025). Subsequently, for a predefined sensed region, is possible to compute some statistical metrics for each TEC Gradient Index component of the N obtained vectors:

- $TEGIX_{mean}$: mean of all the vectors.
- $TEGIX_{\sigma}$: standard deviation.
- $TEGIX_{95p}$: 95th percentile.

Radio-occultation antenna

Differently from the POD antenna, the RO antenna points toward the horizon, sensing the bent GNSS signals refracted by the ionosphere during satellite setting or rising events. RO is a widely used sensing technique employed for the characterization of pressure and density profiles in the troposphere, as well as for the retrieval of electron density profiles of interest to this work. As shown in Fig. 7, the estimation of those profiles starts with the retrieval of the calibrated STEC. The most common inversion technique is the Abel inversion (Teunissen & Montenbruck, 2017) which, under the spherical symmetry assumption, consists in inverting the STEC integral as

$$N_e(r) = -\frac{1}{\pi}\int_r^{r_{\mathrm{LEO}}} \frac{d\big(\mathrm{STEC}(h)\big)}{dh}\frac{dh}{\sqrt{h^2 - r^2}}, \tag{33}$$

where h is the radial distance of the tangent point from Earth's centre, r_{LEO} is the radial distance of the LEO receiver, $\mathrm{STEC}(h)$ is the STEC as a function of the tangent point radial distance and r is the geocentric radius at which N_e is evaluated (Angling et al., 2021), (Shume et al., 2017). In particular, it must be noticed that r exists in the range $min(h) \leq r \leq r_{LEO}$. Then, the resolved integral is

$$N_e(r) = -\frac{1}{\pi}\sum_{i=j}^{I-1}\frac{\Delta(STEC)}{\Delta h}\ln\left(\frac{h_{i+1} + \sqrt{h_{i+1}^2 - r^2}}{h_i + \sqrt{h_i^2 - r^2}}\right), \tag{34}$$

where, $\Delta(STEC) = \mathrm{TEC}_{i+1} - \mathrm{TEC}_i$, $\Delta h = h_{i+1} - h_i$, j is the smallest index such that $h_j \geq r$, and the samples h_i are assumed to be sorted in ascending order to avoid negative argument in the square root. Specifically, it is worth considering 80 km for $min(h)$ as it is the commonly adopted altitude defining the Ionosphere beginning. Another method used to describe the electronic density profile is the so-called *Onion Peeling* (Leitinger et al., 1997), (Shaikh et al., 2014). This

technique models the ionosphere as a set of concentric spherical shells, each characterised by a uniform electron density and by a radius equal to h. A key assumption underlying the method is that the electron density depends only on height, i.e. spherical symmetry is assumed (Shaikh et al., 2014). Rather than using the full STEC, the technique operates on the portion of TEC accumulated along the ray path between r_{LEO} and a minimum altitude of 80 km, referred to as the Limb Total Electron Content (LTEC) (Shaikh et al., 2014). Specifically, for the i-th ray path, LTEC_i is expressed as:

$$\mathrm{LTEC}_i = \sum_{n=i+1}^{N} 2\, L_{in}\, Ne_n + L_{in}\, Ne_i \tag{35}$$

where L_{in} is the path length of the i-th ray inside the n-th shell, N is the total number of shells, Ne_n is the electron density of the n-th shell, and Ne_i is the electron density of the shell at the perigee of the i-th ray. The resulting linear system has a triangular structure and is therefore solved sequentially from the outermost shell inward, allowing the LTEC measurements to be inverted to retrieve the electron density profile $N_e(h)$.

3.7 Cycle slip detection

Cycle slips have been mentioned several times so far, but no detection method has been discussed yet. This step is nonetheless crucial, as it directly affects ROT and ROTI estimation. This processing chain does not implement a dedicated detection technique; instead, one of the receiver outputs listed in Table 1 already carries the key information about phase unlocks. Indeed, the "CumLossCont" parameter is a counter that increments every time a phase discontinuity occurs, whether caused by reacquisition or a cycle slip. Even though the receiver's technical documentation does not disclose the underlying cycle-slip detection algorithm, this parameter serves as a practical proxy for filter reinitialization in the STEC leveling process, as well as for reliable ROT and ROTI estimation. Future developments of the processing chain will nonetheless include dedicated cycle-slip detection algorithms.

4. Pipeline Validation Roadmap

The ELECTRA TEC processing pipeline is being validated through a progressive validation roadmap, shown in Figure 8, moving from numerical simulations to hardware testing on ground, and, finally, to in-orbit data exploitation. This approach is required because the mission output depends not only on the mathematical formulation of TEC retrieval algorithms, but also by several different factors such as the spacecraft attitude and the subsequent visibility geometry with GNSS satellites, the selected sampling strategy and the operational constraints imposed by onboard storage and downlink windows.

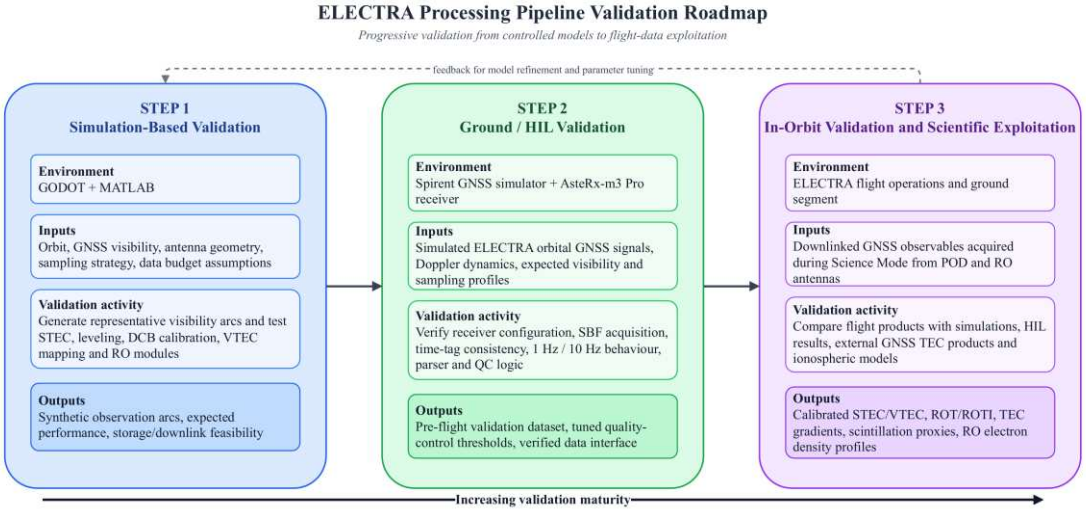


Fig. 8. Validation roadmap of the ELECTRA processing pipeline

4.1 Step 1: Simulations

At the current stage, mission design and performance evaluation are carried out in a controlled simulated environment. The analysis framework relies on GODOT, the ESA Flight Dynamics tool, for orbital and coverage simulations (European Space Agency (ESA) Flight Dynamics, n.d.) . This step is crucial for the definition and design of the data structures that will be used during the mission; in particular, it is necessary to define a data format that can be readily ingested by the processing pipeline. Such simulations present several limitations, most notably the fact that the modelled payload does not reflect the real payload, introducing discrepancies that may be misleading. For this specific reason, Hardware In the Loop (HIL) testing with a proper satellite simulator is necessary.

4.2 Step 2: Ground testing

The second validation step consists of a Hardware In the Loop (HIL) test campaign using a *Spirent* GNSS signal simulator. The objective is to exercise the selected GNSS receiver under a simulated ELECTRA orbital scenario, before the actual flights of the mission. This campaign will reproduce the expected signal conditions, as well as the satellite visibility, the antenna geometry and the sampling configuration associated with the mission.

This step represents the bridge between purely numerical simulations and the operational mission scenario. For instance, it will be used to verify the receiver configuration, the acquisition of the selected SBF observables, the consistency of the time tags, the behaviour of the receiver, as well as the compatibility between the generated data stream and the on-board storage/downlink concept. The same dataset will also be processed by the ground pipeline to validate also the on-ground processing algorithms and the scientific data pipelines developed to achieve the mission objectives.

4.3 Step 3: Validation with orbital data

The final validation step will be performed using data collected during the ELECTRA in-orbit operations. Once the GNSS observables are acquired during *Science Mode*, stored onboard and downlinked during *Transmission Mode*, the complete processing pipeline will be applied to real flight data.

The in-orbit results will first be compared with the expected performance derived from the simulations and the HIL campaigns. This comparison will allow the identification of discrepancies and the connection to the causing factors, such as possible data gaps, real payload behavior and actual ionospheric conditions. The scientific products will then be compared, when possible, with external ionospheric datasets and models, including ground-based GNSS TEC and empirical or assimilative ionospheric models.

5. Conclusions

This paper presented the design of the GNSS data processing pipeline developed for the ELECTRA CubeSat mission, a student-driven 3U platform, conceived to investigate the ionospheric Total Electron Content in LEO using dual-frequency multi-constellation GNSS measurements.

Although the mission has not yet reached the in-orbit data exploitation phase, the pipeline architecture has been defined to account for the main operational constraints of the mission, including discrete science acquisition windows, onboard storage limitations, downlink opportunities, variable sampling rates, and the use of two different antenna geometries. The next development steps will therefore focus on the progressive validation of the processing chain through additional simulations, Hardware In the Loop testing with a GNSS signal simulator, and, finally, processing of the in-orbit measurements collected by ELECTRA.

Once validated with flight data, the resulting dataset will be made available to support scientific investigations on ionospheric dynamics and space-weather effects. In Fig. 7 are also included two further potential outputs: ionospheric tomography and VTEC assimilation into a background model. However, both analyses are limited by the single-satellite nature of ELECTRA. Tomographic reconstruction requires STEC measurements along multiple, geometrically diverse ray paths, which a single receiver cannot provide (Raymond et al., 1994). Similarly, VTEC assimilation into a background model is meaningful only when a spatially dense set of estimates is available, a condition that cannot be met by a single LEO satellite. Both capabilities would therefore require a multi-satellite constellation. In this perspective, ELECTRA represents not only a CubeSat mission for TEC research, but also a pilot case for assessing the scientific value of low-cost small-satellite platforms as part of future distributed ionospheric monitoring systems.

Fundings

This paper did not received any fundings.

Acknowledgment

The authors gratefully acknowledge the ESA for the support provided through *Fly Your Satellite! Design Booster* programme, which has accompanied the ELECTRA mission through its design and review phases. The authors also wish to thank the *Istituto Nazionale di Geofisica e Vulcanologia* (INGV), and in particular Dr. Claudio Cesaroni, for the scientific support provided on ionospheric data processing and interpretation.

References

Abbate, G., Campioli, S., Corpino, S., Stesina, F., Cazacu, D. A., Demoro, D., Tomatis, A., & Di Nardo, L. (2025). Full Functional Test, Data Management, Machine Learning and Automatization of the Cubesat Control Centre: Moving Towards the Operations Phase of an Educational Ground Station. *Proceedings of the 76th International Astronautical Congress*, 51–61. https://doi.org/10.52202/083086-0005

Angling, M. J., Nogués-Correig, O., Nguyen, V., Vetra-Carvalho, S., Bocquet, F.-X., Nordstrom, K., Melville, S. E., Savastano, G., Mohanty, S., & Masters, D. (2021). Sensing the ionosphere with the Spire radio occultation constellation. *Journal of Space Weather and Space Climate*, *11*, 56. https://doi.org/10.1051/swsc/2021040

Ao, C. O., Hajj, G. A., Meehan, T. K., Dong, D., Iijima, B. A., Mannucci, A. J., & Kursinski, E. R. (2009). Rising and setting GPS occultations by use of open-loop tracking. *Journal of Geophysical Research: Atmospheres*, *114*(D4). https://doi.org/10.1029/2008JD010483

Bock, H., Jäggi, A., Švehla, D., Beutler, G., Hugentobler, U., & Visser, P. (2007). Precise orbit determination for the GOCE satellite using GPS. *Advances in Space Research*, *39*(10), 1638–1647. https://doi.org/10.1016/j.asr.2007.02.053

Cahuasquí, J. A., Hoque, M. M., Jakowski, N., Buchert, S., Vasylyev, D., Nykiel, G., David, P., Tagargouste, Y., Kriegel, M., Berdermann, J., & Nielsen, K. (2025). New Swarm products NeGIX and TEGIX for monitoring horizontal ionospheric gradients. *Journal of Space Weather and Space Climate*, *15*, 45. https://doi.org/10.1051/swsc/2025040

Campioli, S., My, C., Belluardo, E., Cortigiano, M. A., Franceschini, A., Abbate, G., Grisolia, M., Taretto, A., Riccardi, F., Fiorina, F., Corpino, S., Giaccone, S., Li Vigni, M., & Tomatis, A. (2025). An Educational 3U CubeSat Mission at Politecnico Di Torino: The ELECTRA Mission for TEC Research and Micro Thruster In-Orbit Testing. *Proceedings of the 76th International Astronautical Congress*, 275–285. https://doi.org/10.52202/083098-0024

Cesaroni, C., Spogli, L., Guerra, M., Ghidoni, R., Ventriglia, V., Minetto, A., Nardin, A., Alfonsi, L., & Dovis, F. (2026). Observing the Earth's Plasmasphere and Ionosphere From the Lunar Surface. *Geophysical Research Letters*, *53*(12). https://doi.org/10.1029/2026GL121811

Cheng, P., & Morton, Y. J. (2025). Observation of Large-Scale Traveling Ionospheric Disturbances in the Topside Ionosphere Using POD TEC From Multiple LEO Satellites Constellations. *Journal of Geophysical Research: Space Physics*, *130*(4). https://doi.org/10.1029/2024JA033293

European Space Agency (ESA) Flight Dynamics. (n.d.). *GODOT: General Orbit Determination and Optimisation Toolkit*. Retrieved October 19, 2026, from https://godot.io.esa.int/

Foelsche, U., & Kirchengast, G. (2002). A simple "geometric" mapping function for the hydrostatic delay at radio frequencies and assessment of its performance. *Geophysical Research Letters*, *29*(10). https://doi.org/10.1029/2001GL013744

Hatch, R. R. (1982). The Synergism of GPS Code and Carrier Measurements. *Proceedings of the Third International Geodetic Symposium on Satellite Doppler Positioning*, 1213–1231.

Hatch, R. R. (1986). Dynamic differential GPS at the centimeter level. *Proceedings of the 4th International Geodetic Symposium on Satellite Positioning*, 1287–1298.

Heine, T. R. P., Moldwin, M. B., Zou, S., Arlas, J., Desai, A., Heidt, B., Mccarty, S., Nastasoiu, A., & Singh, V. (2015). A CubeSat Concept for Multipoint Ionospheric GPS Occultation. *Journal of Small Satellites (JoSS)*, *4*(2), 329–356. www.jossonline.com

Hernández-Pajares, M., Juan, J. M., Sanz, J., García-Fernández, M., & Fernández, F. (2005). Towards a more realistic mapping function. *XXVIII General Assembly of URSI*.

Innerkofler, J., Kirchengast, G., Schwärz, M., Pock, C., Jäggi, A., Andres, Y., & Marquardt, C. (2020). Precise Orbit Determination for Climate Applications of GNSS Radio Occultation including Uncertainty Estimation. *Remote Sensing*, *12*(7), 1180. https://doi.org/10.3390/rs12071180

Jackson, J. E. (1988). *Results from Alouette 1, Explorer 20, Alouette 2, and Explorer 31*.

Jakowski, N., Wehrenpfennig, A., Heise, S., Reigber, Ch., Lühr, H., Grunwaldt, L., & Meehan, T. K. (2002). GPS radio occultation measurements of the ionosphere from CHAMP: Early results. *Geophysical Research Letters*, *29*(10). https://doi.org/10.1029/2001GL014364

Jin, Shuanggen. (2012). *Global Navigation Satellite Systems : Signal, Theory and Applications*. INTECH.

Kashcheyev, A., & Nava, B. (2019). Validation of NeQuick 2 Model Topside Ionosphere and Plasmasphere Electron Content Using COSMIC POD TEC. *Journal of Geophysical Research: Space Physics*, *124*(11), 9525–9536. https://doi.org/10.1029/2019JA026971

Kervalishvili, G., Xiong, C., Stolle, C., Rauberg, J., & van den IJssel, J. (2018). *GOCE High-level Processing Facility GOCE Level 1 and Level 2 Reprocessing Campaign Technical Note Computation of TEC and Rate of TEC Index (ROTI) from GOCE GPS*.

Klaes, K. D., Cohen, M., Buhler, Y., Schlüssel, P., Munro, R., Luntama, J.-P., von Engeln, A., Clérigh, E. Ó., Bonekamp, H., Ackermann, J., & Schmetz, J. (2007). An Introduction to the EUMETSAT Polar system. *Bulletin of the American Meteorological Society*, *88*(7), 1085–1096. https://doi.org/10.1175/BAMS-88-7-1085

Kuang, D., Bar-Sever, Y., Bertiger, W., Desai, S., Haines, B., Iijima, B., Kruizinga, G., Meehan, T. ', & Romans, L. (2001). Precise orbit determination for CHAMP using GPS data from BlackJack receiver. *Proceedings of the Institute of Nav- Igation National Technical Meeting (ION NTM 2001)*.

Lachapelle, G., Hagglund, J., Falkenberg, W., Bellemare, P., Casey, M., & Eaton, M. (1986). GPS Land Kinematic Positioning Experiments. *4th International Geodetic Symposium on Satellite Positioning*, 1327–1344.

Leitinger, R., Ladreiter, H. -P., & Kirchengast, G. (1997). Ionosphere tomography with data from satellite reception of Global Navigation Satellite System signals and ground reception of Navy Navigation Satellite System signals. *Radio Science*, *32*(4), 1657–1669. https://doi.org/10.1029/97RS01027

Liu, L., Morton, Y. J., Wang, Y., & Wu, K.-B. (2022). Arctic TEC Mapping Using Integrated LEO-Based GNSS-R and Ground-Based GNSS Observations: A Simulation Study. *IEEE Transactions on Geoscience and Remote Sensing*, *60*, 1–10. https://doi.org/10.1109/TGRS.2021.3138692

Liu, Z., Gao, Y., & Skone, S. (2005). A study of smoothed TEC precision inferred from GPS measurements. *Earth, Planets and Space*, *57*(11), 999–1007. https://doi.org/10.1186/BF03351880

Luo, X., Gu, S., Lou, Y., Cai, L., & Liu, Z. (2020). Amplitude scintillation index derived from C/N0 measurements released by common geodetic GNSS receivers operating at 1 Hz. *Journal of Geodesy*, *94*(2), 27. https://doi.org/10.1007/s00190-020-01359-7

Montenbruck, O., Hauschild, A., Andres, Y., von Engeln, A., & Marquardt, C. (2013). (Near-)real-time orbit determination for GNSS radio occultation processing. *GPS Solutions*, *17*(2), 199–209. https://doi.org/10.1007/s10291-012-0271-y

Montenbruck, O., Hauschild, A., Langley, R. B., & Siemes, C. (2019). CASSIOPE orbit and attitude determination using commercial off-the-shelf GPS receivers. *GPS Solutions*, *23*(4), 114. https://doi.org/10.1007/s10291-019-0907-2

Morton, Y. T. J., Diggelen, F., Spilker, J. J., Parkinson, B. W., Lo, S., & Gao, G. (Eds.). (2020). *Position, Navigation, and Timing Technologies in the 21st Century*. Wiley. https://doi.org/10.1002/9781119458555

Raymond, T. D., Franke, S. J., & Yeh, K. C. (1994). Ionospheric tomography: its limitations and reconstruction methods. *Journal of Atmospheric and Terrestrial Physics*, *56*(5), 637–657. https://doi.org/10.1016/0021-9169(94)90104-X

Reigber, Ch., Schwitntzer, P., & Luhr, H. (1999). The CHAMP geopotential mission. *Bollettino Di Geofisica Teorica Ed Applicata*, *40*, 285–289.

Ren, X., Chen, J., Zhang, X., Schmidt, M., Li, X., & Zhang, J. (2020). Mapping topside ionospheric vertical electron content from multiple LEO satellites at different orbital altitudes. *Journal of Geodesy*, *94*(9), 86. https://doi.org/10.1007/s00190-020-01415-2

Ren, X., Mei, D., Zhang, X., Freeshah, M., & Xiong, S. (2021). Electron Density Reconstruction by Ionospheric Tomography From the Combination of GNSS and Upcoming LEO Constellations. *Journal of Geophysical Research: Space Physics*, *126*(10). https://doi.org/10.1029/2020JA029074

Ren, X., Zhang, J., Chen, J., & Zhang, X. (2022). Global Ionospheric Modeling Using Multi-GNSS and Upcoming LEO Constellations: Two Methods and Comparison. *IEEE Transactions on Geoscience and Remote Sensing*, *60*, 1–15. https://doi.org/10.1109/TGRS.2021.3050413

Ren, X., Zhang, X., Schmidt, M., Zhao, Z., Chen, J., Zhang, J., & Li, X. (2020). Performance of GNSS Global Ionospheric Modeling Augmented by LEO Constellation. *Earth and Space Science*, *7*(1). https://doi.org/10.1029/2019EA000898

Schreiner, W. S., Weiss, J. P., Anthes, R. A., Braun, J., Chu, V., Fong, J., Hunt, D., Kuo, Y. -H., Meehan, T., Serafino, W., Sjoberg, J., Sokolovskiy, S., Talaat, E., Wee, T. K., & Zeng, Z. (2020). COSMIC-2 Radio Occultation Constellation: First Results. *Geophysical Research Letters*, *47*(4). https://doi.org/10.1029/2019GL086841

Septentrio nv/sa. (2023). *AsteRx-m3 ProBase Firmware v4.14.10 Reference Guide*. www.septentrio.com

Shaikh, M. M., Notarpietro, R., & Nava, B. (2014). The impact of spherical symmetry assumption on radio occultation data inversion in the ionosphere: An assessment study. *Advances in Space Research*, *53*(4), 599–608. https://doi.org/10.1016/j.asr.2013.10.025

Shume, E. B., Vergados, P., Komjathy, A., Langley, R. B., & Durgonics, T. (2017). Electron number density profiles derived from radio occultation on the CASSIOPE spacecraft. *Radio Science*, *52*(9), 1190–1199. https://doi.org/10.1002/2017RS006321

Skone, S. (1998). *Wide Area Ionosphere Grid Modeling in the Auroral Region*.

Straus, P. (2023). *COSMIC-2 Data Products*. https://www.cosmic.ucar.edu/what-we-do/cosmic-2/data

Teunissen, P. J. G., & Montenbruck, O. (Eds.). (2017). *Springer Handbook of Global Navigation Satellite Systems*. Springer International Publishing. https://doi.org/10.1007/978-3-319-42928-1

van den IJssel, J., Forte, B., & Montenbruck, O. (2016). Impact of Swarm GPS receiver updates on POD performance. *Earth, Planets and Space*, *68*(1), 85. https://doi.org/10.1186/s40623-016-0459-4

Weiss, J.-P., Schreiner, W. S., Braun, J. J., Xia-Serafino, W., & Huang, C.-Y. (2022). COSMIC-2 Mission Summary at Three Years in Orbit. *Atmosphere*, *13*(9), 1409. https://doi.org/10.3390/atmos13091409

Wertz, J. Richard., Everett, D. F. ., & Puschell, J. John. (2018). *Space mission engineering : the new SMAD* (J. R. Wertz, D. F. Everett, & J. J. Puschell, Eds.). Microcosm Press.

Wu, M., Guo, P., Xue, J., Wang, Y., Tian, Y., & Wu, J. (2022). Analysis and Empirical Modeling of Ionospheric Horizontal Gradients in the TEC Mapping Onboard LEO Satellites. *IEEE Transactions on Geoscience and Remote Sensing*, *60*, 1–14. https://doi.org/10.1109/TGRS.2022.3188336

Zhong, J., Lei, J., Dou, X., & Yue, X. (2016). Assessment of vertical TEC mapping functions for space-based GNSS observations. *GPS Solutions*, *20*(3), 353–362. https://doi.org/10.1007/s10291-015-0444-6

Zhong, J., Lei, J., Yue, X., & Dou, X. (2016). Determination of Differential Code Bias of GNSS Receiver Onboard Low Earth Orbit Satellite. *IEEE Transactions on Geoscience and Remote Sensing*, *54*(8), 4896–4905. https://doi.org/10.1109/TGRS.2016.2552542